


RESEARCH ARTICLE

Development of hydrogel-based composite scaffolds containing eggshell particles for bone regeneration applications

Nicholas D. Calvert¹  | Scott Proulx¹  | Alejandro Rodriguez-Navarro²  |
Tamer Ahmed¹  | Eric A. Lehoux³  | Maxwell T. Hincke^{1,4}  | Isabelle Catelas^{3,5,6} 

¹Department of Cellular and Molecular Medicine, Faculty of Medicine, University of Ottawa, Ottawa, Ontario, Canada

²Departamento de Mineralogía y Petrología, Universidad de Granada, Granada, Spain

³Department of Mechanical Engineering, Faculty of Engineering, University of Ottawa, Ottawa, Ontario, Canada

⁴Department of Innovation in Medical Education, Faculty of Medicine, University of Ottawa, Ottawa, Ontario, Canada

⁵Department of Surgery, Faculty of Medicine, University of Ottawa, Ottawa, Ontario, Canada

⁶Department of Biochemistry, Microbiology and Immunology, Faculty of Medicine, University of Ottawa, Ottawa, Ontario, Canada

Correspondence

Maxwell T. Hincke, Department of Cellular and Molecular Medicine, Faculty of Medicine, University of Ottawa, Ottawa, Ontario, Canada.
Email: mhincke@uottawa.ca

Isabelle Catelas, Department of Mechanical Engineering, Faculty of Engineering, University of Ottawa, Ottawa, Ontario, Canada.
Email: icatelas@hotmail.com; icatelas@uottawa.ca

Funding information

Egg Farmers of Canada (EFC); Ministerio de Economía y Compatitividad; Natural Sciences and Engineering Research Council of Canada (NSERC); RNM-179 group (Junta de Andalucía, Spain)

Abstract

This study describes the development and characterization of novel composite scaffolds, made of an alginate-chitosan hydrogel matrix containing eggshell (ES) particles, for bone tissue engineering applications. Scaffolds with ES particles, either untreated or treated with phosphoric acid to create a nanotextured particle surface, were compared to scaffolds without particles. Results indicate that the nanotexturing process exposed occluded ES proteins orthologous to those in human bone extracellular matrix. Scaffolds with ES or nanotextured ES (NTES) particles had a higher porosity ($81 \pm 4\%$ and $89 \pm 5\%$, respectively) than scaffolds without particles ($59 \pm 5\%$) ($p = .002$ and $p < .001$, respectively). Scaffolds with NTES particles had a larger median pore size ($113 \mu\text{m}$ [interquartile range [IQ]: $88\text{--}140 \mu\text{m}$]) than scaffolds with ES particles ($94 \mu\text{m}$ [IQ: $75\text{--}112 \mu\text{m}$]) and scaffolds without particles ($99 \mu\text{m}$ [IQ: $74\text{--}135 \mu\text{m}$]) ($p < .001$ and $p = .011$, respectively). The compressive modulus of the scaffolds with ES or NTES particles remained low (3.69 ± 0.70 and 3.14 ± 0.62 kPa, respectively), but these scaffolds were more resistant to deformation following maximum compression than those without particles. Finally, scaffolds with ES or NTES particles allowed better retention of human mesenchymal stem cells during seeding ($53 \pm 12\%$ and $57 \pm 8\%$, respectively, vs. $17 \pm 5\%$ for scaffolds without particles; $p < .001$ in both cases), as well as higher cell viability up to 21 days of culture ($67 \pm 17\%$ and $61 \pm 11\%$, respectively, vs. $15 \pm 7\%$ for scaffolds without particles; $p < .001$ in both cases). In addition, alkaline phosphatase (ALP) activity increased up to $558 \pm 164\%$ on day 21 in the scaffolds with ES particles, and up to $567 \pm 217\%$ on day 14 in the scaffolds with NTES particles ($p = .006$ and $p = .002$, respectively, relative to day 0). Overall, this study shows that the physicochemical properties of the alginate-chitosan hydrogel scaffolds with ES or NTES particles are similar to those of cancellous bone. In addition, scaffolds with particles supported early osteogenic differentiation and therefore represent a promising new bone substitute, especially for non-load bearing applications.

KEYWORDS

alginate, bone substitutes, chitosan, eggshell particles, microstructure, scaffolds, surface modification

This is an open access article under the terms of the [Creative Commons Attribution-NonCommercial-NoDerivs](https://creativecommons.org/licenses/by-nc-nd/4.0/) License, which permits use and distribution in any medium, provided the original work is properly cited, the use is non-commercial and no modifications or adaptations are made.

© 2023 The Authors. *Journal of Biomedical Materials Research Part B: Applied Biomaterials* published by Wiley Periodicals LLC.

1 | INTRODUCTION

Bone defects and loss of bone mass as a result of a disease, fracture, or aging continue to be a problem, with only a few commonly used treatment methods.¹ The autograft procedure, performed over 2 million times worldwide annually, remains the gold standard treatment. Although effective, this procedure is painful for the patient, associated with donor site morbidity, and costly due to long surgical times.^{2,3} Because of these drawbacks, the development of bone graft substitutes has been an intense area of research⁴ and represents a growing market that is projected to reach almost \$5 billion by 2030 in the United States alone.⁵

The design of an optimal bone regeneration biomaterial is guided by the fundamentals of bone biology. Briefly, bone is a calcified tissue, primarily composed of collagen, calcium phosphate, and cells that are organized in cortical and cancellous regions.⁶ The cancellous region is the spongy interior of the bone. It has a high porosity with both large and small pore sizes, and low mechanical strength.^{7,8} The bone marrow, which resides within the cancellous region, contains different growth factors and cell types, including mesenchymal stem cells (MSC), a type of multilineage cells that are precursors of osteoblasts – cells responsible for the deposition of bone extracellular matrix (ECM) and for bone mineralization.⁶ The bone mineralization process, known as osteogenesis, produces apatite (calcium phosphate), the main mineral component of bone.^{9,10} Most biomaterials used for bone regeneration are designed to mimic the cancellous region and support cellular proliferation.¹¹ Porous hydroxyapatite is one of the most commonly used materials clinically. Other apatite materials are derived, for example, from sea coral (e.g., *Porites* sp.) through hydrothermal exchange.¹² These materials have a composition and porosity very similar to that of cancellous bone.¹² Calcium carbonate biominerals (e.g., nacre from mollusk shells) have also been used as bone grafts because of their osteoinductive properties and biocompatibility.^{13–15}

Chicken eggshell (ES) is another interesting calcium carbonate biomineral to explore as an alternative bone graft material. ES is a thin mineral layer composed primarily of calcite (ca. 94% by mass).¹⁶ While human bone is composed primarily of apatite (ca. 65% by mass), both calcite and apatite are calcium-based minerals. In addition, ES contains a matrix of occluded proteins that include important bone ECM proteins such as collagen, osteopontin, matrix extracellular phosphoglycoprotein, and serum albumin.^{17–19} Because of these properties, ES has been evaluated as a bone regeneration material in different applications and, in particular, as a filler or packing material for maxillofacial and cranial fractures and defects.^{20,21} In addition, ES calcium carbonate minerals (e.g., calcite, aragonite) can be precursors of synthetic hydroxyapatite, and ES particles have been incorporated into 3D-printed polymer scaffolds or used in conjunction with acids to form a cement.^{22–25} Finally, ES-derived calcium carbonate has been shown to be osteoinductive in vivo.^{20,26} Nevertheless, the use of ES alone as a bone regeneration material has had limited success, probably because of its low porosity and small average pore size.

Hydrogels (e.g., alginate, chitosan), considered to be non-toxic, have also been widely used in bone regeneration applications.^{27–30} These polymeric networks are able to swell and absorb water into

their void space via hydrogen-bonds formed between water and the polymer.³¹ This swelling behavior is critical in tissue regeneration because the material must reach an equilibrium with its fluidic environment.³² In addition, both alginate and chitosan hydrogels can be tailored to have properties (e.g., porosity and pore size) similar to those of cancellous bone in order to maximize MSC viability,^{33,34} and ES particles can be integrated into a alginate-chitosan scaffold, thereby creating a porous mineral-organic composite material with osteogenic properties (provided by the ES particles).³⁵ For example, a recent study³⁶ showed the osteogenic potential of a gelatin metacrylate scaffold with embedded micronized ES particles on pre-osteoblasts in vitro, as well as in vivo in a rat model.

Previous studies have described the generation of nanotextured ES surfaces that were subsequently imprinted onto a polydimethylsiloxane surface.³⁷ Nanotextured surfaces are surfaces covered with nanometer-scale topographical features that have been shown to affect cellular adhesion, proliferation, and differentiation.^{38,39} More specifically, rough and disordered nanotextured surfaces have been shown to induce differentiation of MSC by causing an uneven distribution of their cytoskeleton.⁴⁰ In addition, acid etching of the ES particle surface to induce nanotexturing may also expose occluded ES proteins orthologous to those found in human bone (e.g., collagen, osteopontin), and facilitate the formation of calcium minerals.^{18,19} The combination of these features could further promote MSC differentiation.

The objectives of this study were to: 1. Design and characterize alginate-chitosan hydrogel scaffolds with ES or NTES particles; and 2. Evaluate the osteoconductive properties of these scaffolds and compare them to those of scaffolds without particles.

2 | MATERIALS AND METHODS

2.1 | Preparation and characterization of ES and NTES particles

2.1.1 | Preparation of ES and NTES particles

White eggs from Lohmann White Leghorn hens (Burnbrae Farms, Lyn, ON) were opened at the sharp end using a rotary saw. The content was discarded, and the ES was washed (both sides) 3 times with ASTM Type I water and 3 times with Dulbecco's phosphate-buffered saline without magnesium and calcium (PBS; ThermoFisher Scientific, Waltham, MA). The ES was then cut in half using a rotary saw, incubated in pre-warmed (40°C) 0.268 M NaOCl for 15 min with constant stirring to remove the surface cuticle and inner ES membranes, and rinsed thoroughly and sequentially with ASTM Type I water and PBS. After overnight air-drying at room temperature, the ES halves were manually ground for 60 s using a 350-mL porcelain mortar and pestle (CoorsTek, Golden, CO, catalog numbers 52211 and 60320, respectively), and the resulting powder was sieved (Keck Sieve Shaker Kit, pore size range: 229 μm – 381 μm ; Cole-Parmer, Montreal, QC) (see eggshell particle-size analysis in [Supplemental Material; Section 1](#)). The ES particles were stored at 4°C until use.

ES particles were then subjected to an acid treatment to produce nanotextured ES (NTES) particles. Particles (5 mg) were stirred in 1 mL of 0.250 M phosphoric acid for 10 min at room temperature, collected by vacuum filtration using filter paper (Whatman Grade 1 Qualitative Filter Paper; Cytiva, Marlborough, MA), and washed 3 times with ASTM Type I water, 3 times with PBS, and 3 more times with ASTM Type I water. The resulting NTES particles were air-dried overnight at room temperature and stored at 4°C until use.

2.1.2 | Surface topography and chemical analysis of ES and NTES particles

The surface topography of ES and NTES particles was analyzed by scanning electron microscopy (SEM) using a SEM microscope (Vega-II XMU SEM; TESCAN, Brno, Czech Republic) at an accelerating voltage of 20.0 kV after samples were gold sputter-coated for 5 min under vacuum. The elemental composition of the particle surface was analyzed by energy-dispersive X-ray spectroscopy (EDS) using an EDS spectrometer (INCA EDS detection system; Oxford Instruments, Abingdon, United Kingdom).

To identify the presence of exposed constituents on the particle surface, Fourier-transformed infrared (FTIR) attenuated total reflection (ATR) spectroscopy was performed on dry ES and NTES particles using an FTIR spectrometer (FT/IR-6200, JASCO Analytical Instruments, Tokyo, Japan) over a wavenumber range of 4000–400 cm⁻¹.

2.2 | Preparation and characterization of the scaffolds

2.2.1 | Scaffold preparation

Sodium alginate (from brown seaweed, $\bar{M}_w = 120\text{--}190$ kDa; MilliporeSigma, Burlington, MA) was dissolved in ASTM Type I water to prepare a 2% (w/v) solution. Chitosan (75%–85% deacetylated, $\bar{M}_w = 50\text{--}190$ kDa; MilliporeSigma) was dissolved in 3% (v/v) acetic acid (ThermoFisher Scientific) to prepare a 2% (w/v) solution. An aliquot (750 μL) of sodium alginate solution was added into a paraffin embedding mold (Peel-A-Way; 22 mm length \times 22 mm width \times 20 mm depth; Polysciences, Warrington, PA). Particles (ES or NTES, 20% [w/v]) were added to the sodium alginate solution and mixed manually with a metal stir-stick until homogeneously distributed. This was the highest concentration of particles that did not affect the pore structure of the final scaffold (data not shown). An aliquot (750 μL) of chitosan solution was then added to the sodium alginate solution containing the particles and was mixed to homogeneity with a metal stir-stick. Finally, 30% (v/v) glutaraldehyde (1.5 μL ; 0.03% [v/v] final concentration) was added to the polymer mixture with particles and mixed thoroughly to initiate cross-linking. Scaffolds without particles (blank) were prepared following the same procedure, except that the particles were omitted. The molds were placed on a directional freezing apparatus (custom-made) at -20°C for 24 h. Only the bottom of the molds was in contact with the freezing stage to facilitate unidirectional ice crystal growth. The frozen scaffold blocks were then placed in a freeze-drying flask

(Labconco; Kansas City, MO) and kept in a closed-cell extruded polystyrene foam box containing dry ice and gel packs to maintain freezing temperatures in a freeze-dryer (Labconco) during the 24-h lyophilization process. After lyophilization, 6-mm diameter scaffolds were extracted from the blocks using a histology punch (Integra LifeSciences, Princeton, NJ), and stored at room temperature in a desiccator until use.

2.2.2 | Scaffold porosity measurements

The porosity of all scaffolds was evaluated using a swelling test and was determined by measuring the final volume and the increase in mass of initially dry scaffolds after a 30-min incubation in PBS at 37°C. Scaffolds were weighed before and after the incubation and their dimensions were measured using a digital caliper (Traceable, S/N 140408171; Fisher Scientific). Excess fluid on the scaffold surface was removed by dabbing the surface with a delicate task wiper (Kimberly-Clark, Roswell, GA). The porosity percentage, that is, the volume of the empty pores being filled with PBS, was calculated using Equation 1:

$$\text{Porosity (\%)} = \frac{\left(\frac{\rho_{\text{PBS}}}{\Delta M_s}\right) V_s}{V_s} \times 100 \quad (1)$$

where ρ_{PBS} is the density of the PBS solution, ΔM_s is the change in scaffold mass, and V_s is the volume of the wet scaffold.

It should be noted that the swelling test, which consists of measuring the increase in mass following immersion of the scaffold in PBS, may lead to a small overestimation of the overall porosity due to fluid absorption by the polymeric matrix. This method is, however, commonly used to evaluate the porosity of polymeric scaffolds.^{41,42}

2.2.3 | Scaffold microstructure and pore size analysis

Freeze-dried scaffolds ($n = 3$ for each type) were sectioned perpendicular and parallel to their z-axis (i.e., perpendicular and parallel to the direction of ice crystal growth) using a surgical scalpel (blade size 11). The cross-sectional surfaces were then gold sputter-coated and analyzed using SEM, as described above, for scaffold characterization. Pore sizes of both cross-sectional surfaces were measured using image analysis of secondary electron SEM micrographs (2 micrographs per scaffold) with ImageJ software (FUJI, NIH). The size of 25 randomly selected pores on each cross-sectional image (total of 50 pores per scaffold) were measured. Finally, the morphology of the scaffold microstructure was evaluated qualitatively through visual examination of SEM micrographs (two per scaffold replicate).

2.2.4 | Scaffold compressive modulus measurements

The compressive modulus (CM) of the scaffolds was determined using a protocol adapted from Bas et al.⁴³ Testing was performed on scaffolds equilibrated in PBS at 37°C for 30 min. The temperature was

maintained at 37°C during testing using a heating plate. Scaffolds were subjected to unconfined compression testing using a universal testing machine (UTM; MTS Sintech 1G; MTS Systems Corporation, Eden Prairie, MN) with a 5N load cell. A compressive strain of ca. 30% of the scaffold original height was applied at a displacement rate of 0.01 mm/s. The CM was determined from the slope of the linear region of the stress-strain curves between 10% and 15% strain. The height of each scaffold was measured before and immediately after testing using a digital caliper to detect damage to the scaffold microstructure.

2.2.5 | Scaffold stability evaluation

To evaluate hydrolytic degradation, the scaffolds were placed into paraffin embedding molds (Peel-A-Way; Polysciences), submerged in 2 mL of PBS, and incubated at 37°C in a humidified atmosphere of 5% CO₂ and 95% air for 21 days. Scaffolds were removed from the incubator every 7 days, patted dry with a delicate task wiper to remove excess fluid, and placed in a 96-well microplate (Corning; Tewksbury, MA). Absorbance of the scaffolds was then measured at a wavelength of 590 nm using a plate reader (Eon; BioTek, Winooski, VT) to monitor possible loss of scaffold structure. A decrease in absorbance compared to day 0 was attributed to loss of scaffold microstructure due to hydrolytic degradation. Scaffold dimensions on days 0 and 21 were also measured using a digital caliper to detect changes relative to the original volume (i.e., on day 0) and correlate degradation with loss in scaffold volume.

2.2.6 | Analysis of particle distribution in the scaffolds

Freeze-dried scaffolds ($n = 3$ for each type) were sectioned perpendicular and parallel to their z-axis using a surgical scalpel (as described above). The cross-sectional surfaces were then gold sputter-coated and imaged using backscattered electron SEM to visualize the ES particles within the polymeric matrix. In addition, particle distribution within the scaffolds was qualitatively evaluated using a micro-computed tomography scanner (μ CT scanner, Skyscan 1174; Skyscan, Antwerp, Belgium). Images of scaffolds were acquired using unfiltered X-rays, at an X-ray tube voltage of 37 kV and current of 648 μ A. An image was acquired every 0.7°, through 180° of rotation. Images from each rotation were used to reconstruct a three-dimensional (3D) model with NRecon software 1.6.10.2 (Micro Photonics Inc.; Allentown, PA). Particle distribution was assessed visually by examining the 3D models to evaluate qualitatively the homogeneity of the distribution throughout the scaffolds.

2.3 | Evaluation of scaffold osteoconductive properties

2.3.1 | Scaffold cell seeding

Freeze-dried scaffolds were sterilized by overnight incubation in 70% (v/v) ethanol under cell culture conditions (37°C, in a humidified

atmosphere of 5% CO₂ and 95% air). The scaffolds were then washed three times with PBS pre-warmed to 37°C, and submerged in differentiation culture medium (DCM; ca. 50 mL) composed of Eagle's minimum essential medium, alpha modification with nucleosides (α MEM; Life Technologies, Carlsbad, CA) supplemented with 10% (v/v) heat-inactivated fetal bovine serum (FBS; MilliporeSigma), 10 nM dexamethasone (MilliporeSigma), 20 μ M ascorbic acid (MilliporeSigma), 50 mM β -glycerophosphate (MilliporeSigma), 100 U/mL penicillin and 0.1 mg/mL streptomycin (Life Technologies). Finally, the scaffolds were incubated overnight under cell culture conditions.

Fifth passage single-donor MSC from four different lots (three from American Type Culture Collection [ATCC], Manassas, VA, and one from Cellular Engineering Technologies [CET], Coralville, IA) were resuspended in DCM at ca. 8350 cells/ μ L so that a total of ca. 250,000 cells were seeded in each cylindrical scaffold after depositing 12 aliquots (2.5 μ L each) of cell suspension onto each scaffold. More specifically, 2.5 μ L of MSC suspension were pipetted onto the surface of the scaffolds in two randomly selected areas, followed by a 30-min incubation under cell culture conditions. This seeding step was repeated three times and the scaffolds were incubated for 1 h. The entire procedure was then repeated on the other side of the scaffolds. Finally, the scaffolds were incubated for 1.5 h under cell culture conditions, transferred into a 48-well polystyrene plate (Corning), submerged in DCM, and incubated overnight under cell culture conditions.

The scaffolds (with ES particles, NTES particles or no particles; $n = 3$ for each type) were then transferred into cell culture inserts (0.4- μ m pore size; polycarbonate membrane, ThermoFisher Scientific) that were placed inside the wells of a 24-well plate (Corning) to improve nutrient diffusion.⁴⁴ Both the cell culture inserts and wells of the plate were filled with DCM to submerge the scaffolds (1 mL DCM in each well, 0.25 mL DCM in each insert) that were then incubated for up to 21 days under cell culture conditions. DCM was replaced every 2 days.

2.3.2 | MSC retention and viability in the scaffolds

MSC retention (on day 0, i.e., immediately after seeding) and viability (on days 7, 14, and 21) in the different scaffold types ($n = 3$ for each) were evaluated using a viability dye (AlamarBlue cell viability reagent; ThermoFisher Scientific). Scaffolds at each timepoint were washed thoroughly with pre-warmed (37°C) DCM, then bisected with a scalpel. Both halves of the scaffolds were incubated in DCM, supplemented with AlamarBlue cell viability reagent (1X), for 3 h under cell culture conditions. At the end of the incubation, an aliquot (100 μ L) of each sample suspension was added to a 96-well black-walled, clear bottom polystyrene microplate (Corning), and fluorescence was measured at excitation/emission wavelengths of 530 nm/590 nm using a fluorescence plate reader (Eon, BioTek). Cell retention (on day 0) and cell viability (on days 7, 14, and 21) percentages were calculated from the number of viable cells in the scaffolds (i.e., the sum of the numbers in each half) using a standard curve generated with known numbers of MSC.

2.3.3 | Alkaline phosphatase activity in the scaffolds

At each time point, one of the scaffold halves ($n = 3$ for each scaffold type) was washed with 1 mL of ice-cold PBS, then incubated in 150 μ L of ice-cold lysis buffer (CytoBuster protein extraction reagent [MilliporeSigma] supplemented with a protease inhibitor cocktail [cOmplete without EDTA; Roche, Basel, Switzerland], as per the manufacturer's instructions) for 30 min on ice, and mixed on a tube-shaker (MT-400, Tomy Digital Biology, Tokyo, Japan) for 5 min at 4°C. The scaffold halves were then centrifuged (16,500 $\times g$ for 25 min at 4°C) to sediment scaffold and cellular debris.

Aliquots (50 μ L/well) of the lysate supernatants were added to a 96-well polystyrene microplate (Corning), followed by alkaline phosphatase (ALP) assay buffer (100 μ L/well) containing 100 mM diethanolamine (MilliporeSigma), 0.5 mM $MgCl_2$ (MilliporeSigma), and 2 mM para-nitrophenylphosphate (ThermoFisher Scientific), adjusted to pH 9.8 with 6 M HCl. The microplate was incubated 1 h in the dark at room temperature. At the end of the incubation, 2 N NaOH (50 μ L/well) was added to stop the reaction. Absorbance was measured at a wavelength of 405 nm using a plate reader (Eon, BioTek) and converted to ALP activity using a standard curve prepared with commercial ALP of known activity (Worthington Biochemical, Lakewood, NJ). ALP activity was then normalized to the number of viable cells in the scaffold (determined using alamarBlue cell viability reagent), as opposed to total protein concentration to avoid interference from FBS proteins from the culture medium since cells were lysed directly in the scaffolds. Since osteogenic differentiation has been shown to increase the metabolic activity of MSC⁴⁵, a correction factor (1.5) was

empirically determined (data not shown) and applied to the normalized ALP activity data from days 14 and 21 to account for the increased rate of metabolism (i.e., reduction) of the alamarBlue dye used to normalize enzymatic activity to cell number.

2.4 | Statistical analysis

Statistical analysis of the physicochemical data was performed using SPSS v23 (IBM; Armonk, NY). The data were assumed to meet the

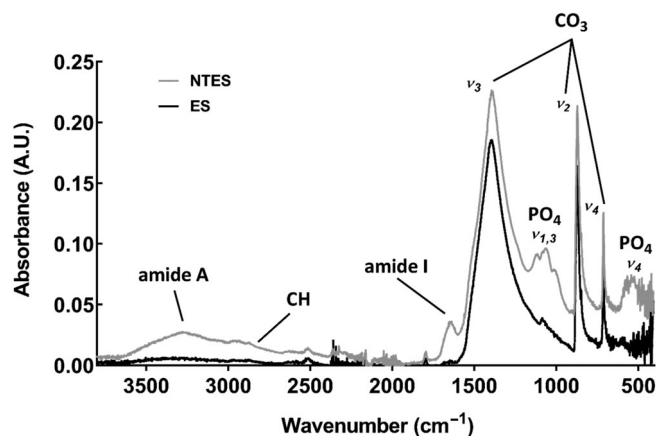


FIGURE 2 Fourier-transformed infrared (FTIR) spectroscopy of eggshell (ES) and nanotextured eggshell (NTES) particles. FTIR analysis was performed to characterize the surface constituents on ES particles before (black) and after (gray) treatment with 0.250 M phosphoric acid.

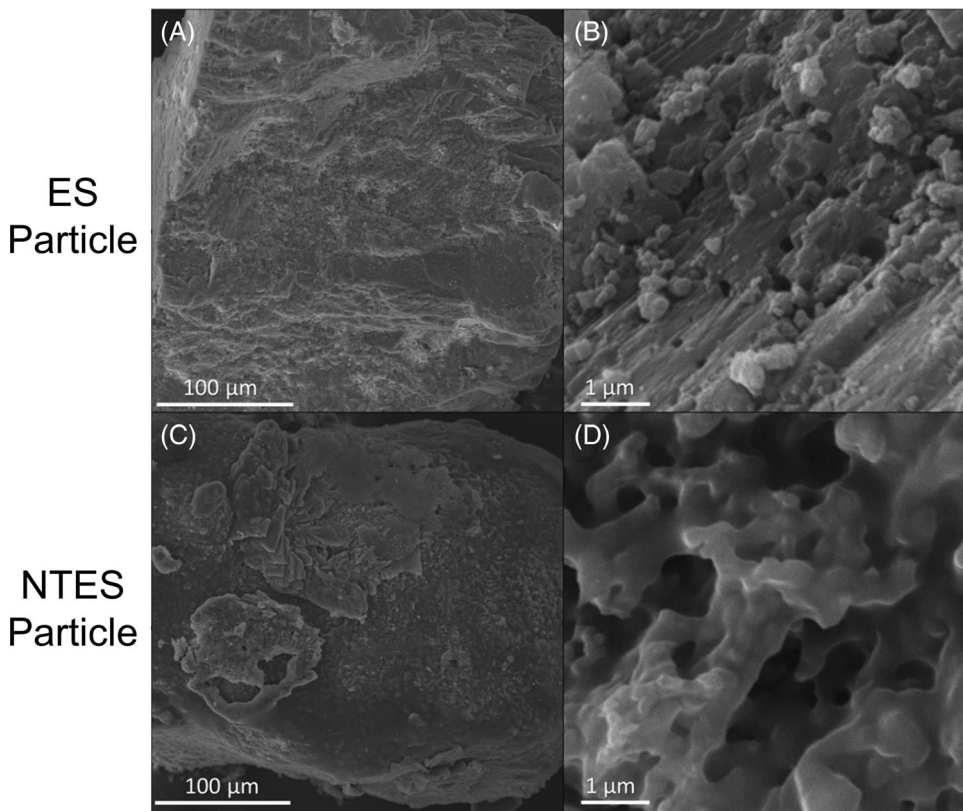


FIGURE 1 Representative scanning electron microscopy micrographs of eggshell (ES) particles before (A, B) and after (C, D) phosphoric acid treatment. Particles were treated with 0.250 M phosphoric acid to produce a surface nanotexture (NTES particles). Magnification: 100 \times (A, C) and 3000 \times (B, D).

assumption of normality (for parametric tests), and Levene's test was used to determine if the assumption of homogeneity of variance was met. Porosity and compressive modulus measurements were analyzed using a one-way analysis of variance (ANOVA) followed by the Tukey post hoc test. Pore size distribution was analyzed using the Kruskal-Wallis test followed by Dunn's post hoc test with a Benjamini-Hochberg correction for multiple comparisons. Scaffold degradation data were analyzed using a two-way ANOVA followed by the Tukey post hoc test. $p < .05$ was considered significant. Data are presented as mean \pm standard deviation (SD) or median with interquartile range, as appropriate.

Statistical analysis of the cellular data was performed using R Statistical Software v3.5.2.⁴⁶ Levene's test and visual analysis of quantile-quantile (QQ) plots were used to determine if the assumption of homogeneity of variance was met. All statistical analyses were performed using a mixed linear model with cell lot as a random factor and scaffold and/or time point as fixed factor(s). Pairwise comparisons were performed using the Tukey post hoc test with a single-step adjustment. All data are presented as mean \pm standard error of the mean (SEM).

3 | RESULTS

3.1 | Characterization of ES and NTES particles

The particle surface before and after acid treatment was visualized using SEM (Figure 1) to assess the morphology of the untreated

particle surface and evaluate the effects of the phosphoric acid treatment. The surface of the untreated ES particles showed interspersed protrusions, pores, and fine striations at high

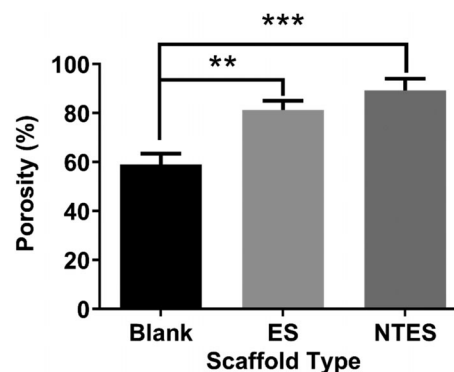


FIGURE 4 Porosity of scaffolds without particles (blank), or with eggshell (ES) or nanotextured eggshell (NTES) particles. Dry scaffolds were submerged in Dulbecco's phosphate-buffered saline under cell culture conditions (37°C, humidified atmosphere of 5% CO₂ and 95% air) for 30 min. Scaffold volume and mass were measured before and after the incubation to determine the scaffold porosity based on the measurements of the final volume and increase in mass. Data are presented as means \pm SD of three independently prepared scaffolds of each type. Statistical analysis was performed using a one-way ANOVA followed by the Tukey post hoc test. A double asterisk (**) and a triple asterisk (***) indicate a significant difference with $p < .01$ and $p < .001$, respectively.

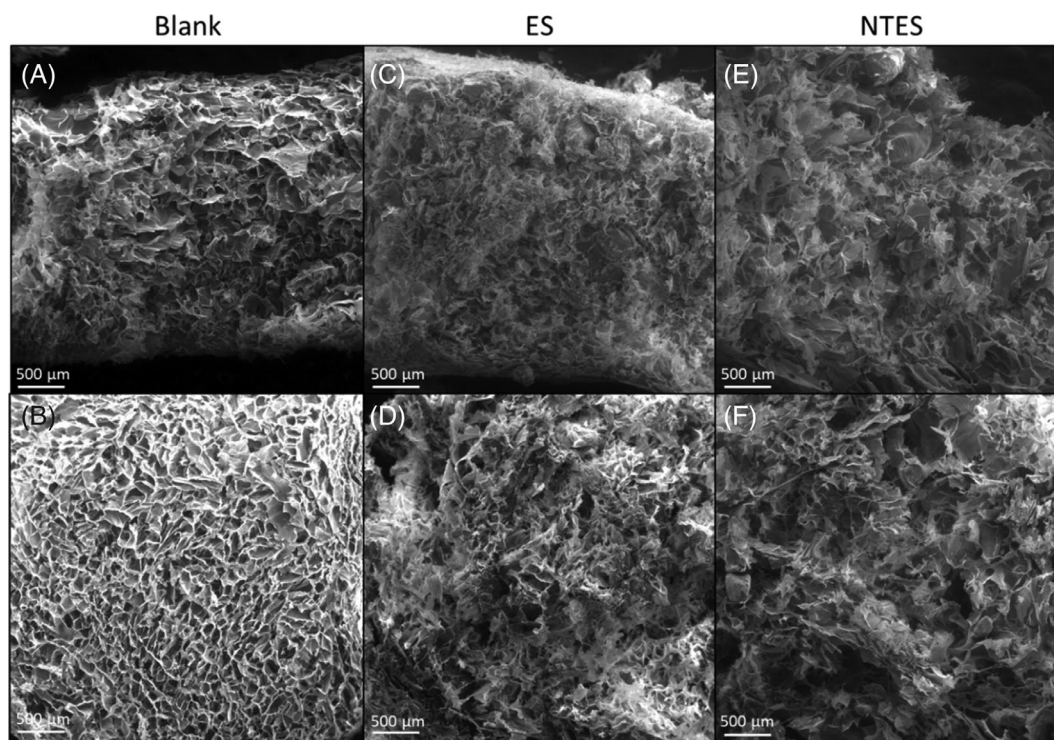


FIGURE 3 Representative secondary-electron micrographs of scaffolds without particles (blank), or with eggshell (ES) or nanotextured eggshell (NTES) particles. Scaffolds were cut either perpendicular (A, C, E) or parallel (B, D, F) to the z-axis (i.e., parallel to the direction of ice crystal growth) and imaged using scanning electron microscopy to observe their microstructure in both planes. Magnification: 100 \times .

magnification (Figure 1A,B). After the acid treatment, the surface of the particles showed granular deposits (Figure 1C) and displayed a distinctly different surface morphology, with randomly distributed patterns of grooves, ridges, and pores (Figure 1D). This rough and more porous surface texture at the submicron scale demonstrates the nanotexturing effect of the acid treatment.

EDS analysis was performed to detect differences in the elemental composition of the particle surface. The elemental composition of ES and NTES particles was similar and included mainly oxygen, calcium, and carbon, as well as traces of magnesium (data not shown). EDS analysis of the granular deposits on the surface of the NTES particles showed higher peaks for oxygen and carbon as well as a smaller peak for calcium, compared to the surface of untreated ES particles. Importantly, deposits,

which also contained phosphorous, were detected only on the surface of NTES particles.

FTIR analysis revealed that the spectra were overall similar for both ES and NTES particles (Figure 2) and showed a broad absorption band centered at 1390 cm^{-1} (asymmetric stretching vibrational mode [ν_3]) as well as two sharp peaks at 873 cm^{-1} (out-of-plane bending [ν_2]) and 713 cm^{-1} (in-plane bending [ν_4]), characteristic of carbonate bands from calcite. However, the spectrum for NTES particles also displayed a doublet band around 1000 cm^{-1} (symmetric and asymmetric stretching [$\nu_{1,3}$]) and a singlet band around 500 cm^{-1} (ν_4) (both attributed to phosphate groups), in addition to a band around 1650 cm^{-1} (amide I region) and a broad band ranging from around 3500 to 2800 cm^{-1} (amide A region).

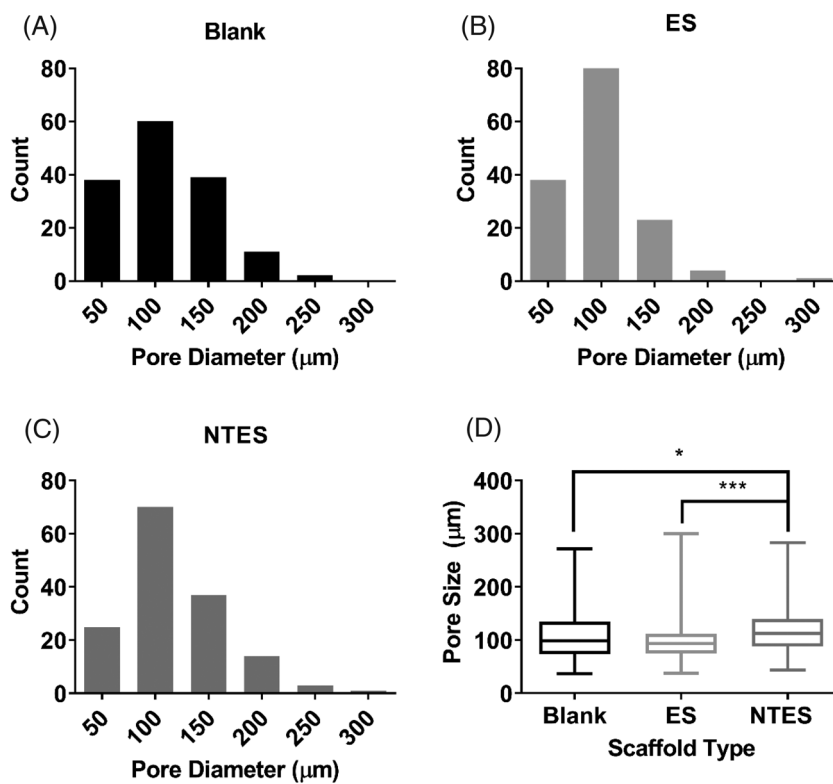


FIGURE 5 Distributions of the scaffold pore sizes: (A) Scaffolds without particles (blank); (B) Scaffolds with eggshell (ES) particles; (C) Scaffolds with nanotextured eggshell (NTES) particles; (D) Comparison of the pore size distributions. Data are presented as binned pore size distributions (A–C) and box-and-whisker plots (D) with median (horizontal line), interquartile range (top and bottom of boxes), and minimum/maximum range (tails) of three independent pooled experiments for each scaffold type (50 measurements for each experiment). Statistical analysis was performed using the Kruskal–Wallis test followed by Dunn's post hoc test with a Benjamini–Hochberg correction for multiple comparisons. An asterisk (*) and a triple asterisk (***) indicate a significant difference with $p < .05$ and $p < .001$, respectively.

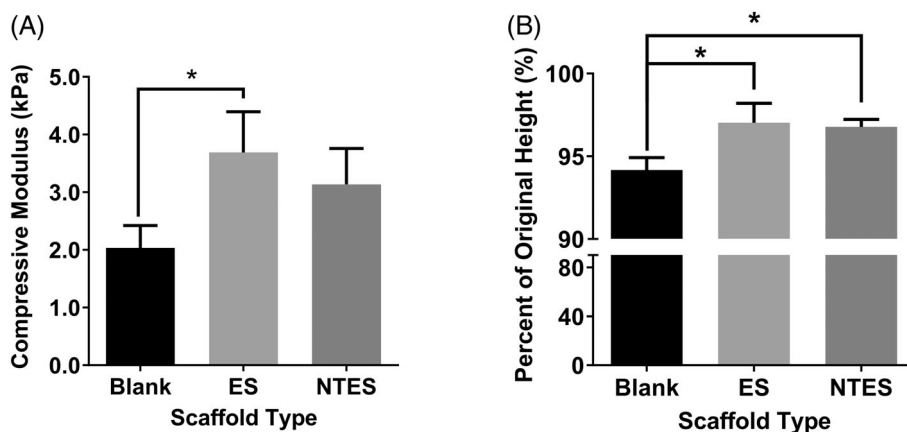


FIGURE 6 Compression testing of scaffolds without particles (blank), or with eggshell (ES) or nanotextured eggshell (NTES) particles: (A) Compressive modulus; and (B) Percent of original height (i.e., scaffold height recovery) after compression tests. Data are presented as means \pm SD of three independently prepared scaffolds of each type. Statistical analysis was performed using a one-way ANOVA followed by the Tukey post hoc test. An asterisk (*) indicates a significant difference with $p < .05$.

3.2 | Characterization of the scaffolds

3.2.1 | Scaffold microstructure, porosity, and pore size

Microstructure analysis of the scaffolds without ES particles (Figure 3A,B) revealed ordered and consistently spaced pores. The inclusion of either ES (Figure 3C,D) or NTES (Figure 3E,F) particles

resulted in scaffolds having a more disorganized and randomly distributed pore structure. In addition, the presence of particles increased the porosity of the scaffolds ($81 \pm 4\%$ and $89 \pm 5\%$ with ES and NTES particles, respectively), relative to the scaffolds without particles ($59 \pm 5\%$) ($p = .002$ and $p < .001$, respectively; Figure 4).

Pore size distributions of all scaffolds were non-gaussian (Figure 5), with the majority of the pores having a diameter between 50 and 150 μm . Scaffold pore sizes were very similar in the

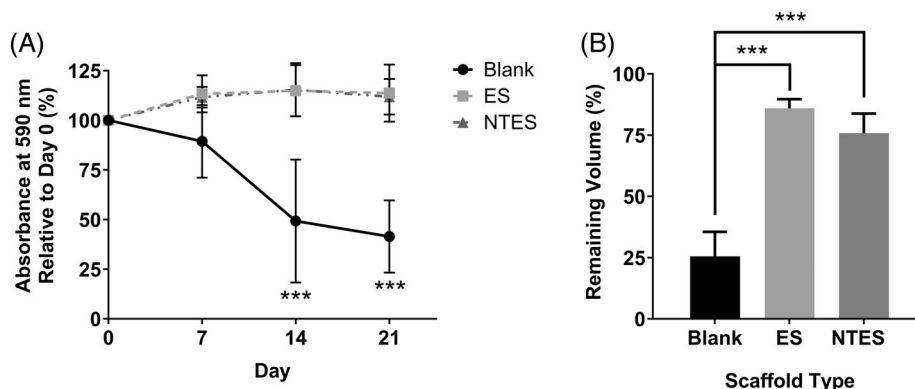


FIGURE 7 Hydrolytic degradation of scaffolds without particles (blank), or with eggshell (ES) or nanotextured eggshell (NTES) particles in phosphate-buffered saline at 37°C: (A) Change in the absorbance (590 nm) of the scaffolds; (B) Remaining volume (reflecting the change in the total scaffold volume) after 21 days. Data are presented as means \pm SD of three independently prepared scaffolds of each type. Statistical analysis was performed using a two-way ANOVA followed by the Tukey post hoc test (A), and a one-way ANOVA followed by the Tukey post hoc test (B). A triple asterisk (***) indicates a significant difference with $p < .001$.

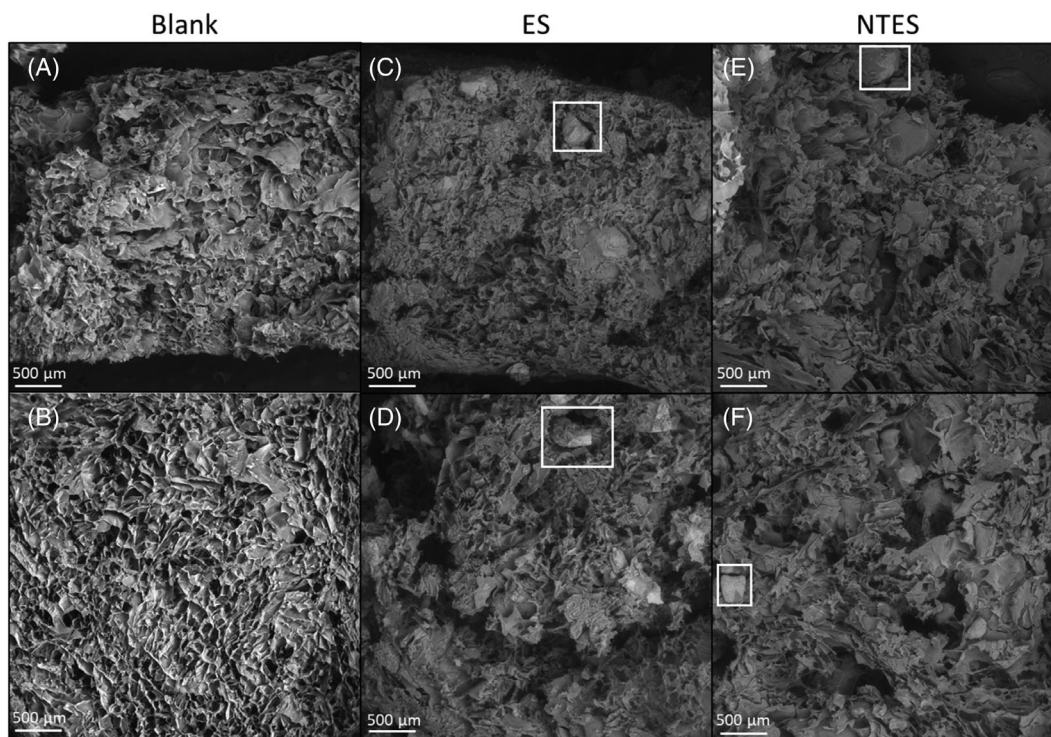


FIGURE 8 Representative backscattered-electron micrographs of scaffolds without particles (blank), or with eggshell (ES) or nanotextured eggshell (NTES) particles. Scaffolds were cut either perpendicular (A, C, E) or parallel (B, D, F) to the z-axis (i.e., parallel to the direction of ice crystal growth) and imaged using scanning electron microscopy to visualize the particles in both planes. White boxes indicate examples of visible ES or NTES particles. Magnification: 100 \times .

perpendicular and parallel cross-sections. Therefore, the data from both directions were pooled. The scaffolds containing NTES particles had a larger median pore size (113 μm [interquartile range [IQ]: 88–140 μm]) than the scaffolds with ES particles (94 μm [IQ]: 75–112 μm) and the scaffolds without particles (99 μm [IQ]: 74–135 μm) ($p < .001$ and $p = .011$, respectively).

3.2.2 | Scaffold compressive modulus

Scaffolds were subjected to unconfined compression testing to determine their CM (Figure 6A). The scaffolds with ES particles had a slightly higher CM than the scaffolds without particles (3.69 ± 0.70 vs. 2.03 ± 0.39 kPa, respectively; $p = .031$). Nevertheless, the CM of the scaffolds with NTES particles (3.14 ± 0.62 kPa) was not significantly different from that of the scaffolds without particles.

The height of the scaffolds before and after testing was also measured as an evaluation of scaffold resiliency, with any permanent change in height from compression reflecting test-induced damage to the scaffold microstructure (Figure 6B). The height recovery of the scaffolds with either ES or NTES particles was greater than that of the scaffolds without particles ($97 \pm 1\%$ for both the scaffolds with ES or NTES particles vs. $94 \pm 1\%$ for the scaffolds without particles; $p = .015$ and $p = .022$, respectively).

3.2.3 | Scaffold stability

Scaffold resistance to hydrolytic degradation was evaluated over 21 days in PBS at 37°C (Figure 7A). Changes in absorbance at a wavelength of 590 nm were attributed to a loss of scaffold microstructure due to hydrolysis. No significant change in absorbance was observed from day 0 to day 21 for the scaffolds with either ES or NTES particles. In contrast, the absorbance of the scaffolds without particles was lower on days 14 and 21 than on day 0 ($49 \pm 31\%$ and $41 \pm 18\%$, respectively, relative to day 0; $p < .001$ in both cases). The volume of each scaffold was also measured on day 0 and day 21 as another indication of scaffold degradation. Results on day 21 showed that the scaffolds with ES or NTES particles retained a higher percentage of their initial volume, compared to the scaffolds without particles ($86 \pm 4\%$ and $76 \pm 8\%$, respectively, vs. $26 \pm 10\%$; $p < .001$ in both cases) (Figure 7B).

3.2.4 | Particle distribution in the scaffolds

The distribution of ES or NTES particles in the scaffolds was evaluated qualitatively using backscattered electron SEM imaging (Figure 8) as well as μCT imaging (Figure 9). The particles appeared to be homogeneously distributed throughout the scaffolds. μCT imaging of the scaffolds without particles (Figure 9A,B) showed a faint signal from the scaffold polymers that was not detected on the images of the scaffolds with ES or NTES particles because of the much greater signal intensity of the particles.

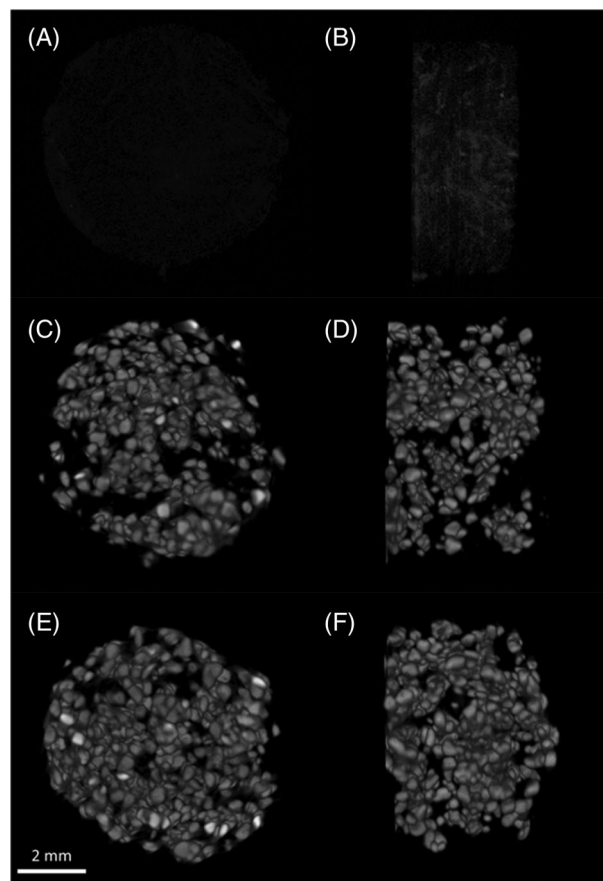


FIGURE 9 Micro-computed tomography (μCT) analysis of the particle distribution within the scaffolds. μCT analysis was performed on scaffolds without particles (A, B), with eggshell (ES) particles (C, D), or with nanotextured eggshell (NTES) particles (E, F). Images show top-down view (A, C, E) or side-view (B, D, F) of three-dimensional reconstructions.

3.3 | Evaluation of scaffold osteoconductive properties

3.3.1 | MSC retention and viability in the scaffolds

MSC retention in the scaffolds on day 0 (after seeding) was measured using alamarBlue (Figure 10A). Results showed that the inclusion of either ES or NTES particles into the scaffolds increased cell retention ($53 \pm 12\%$ and $57 \pm 8\%$ for scaffolds with ES and NTES particles, respectively, vs. $17 \pm 5\%$ for scaffolds without particles; $p < .001$ in both cases).

MSC viability was also evaluated every 7 days over the 21-day culture period (Figure 10B). The scaffolds with ES or NTES particles had a higher percentage of viable cells than the scaffolds without particles up to 21 days of culture ($67 \pm 17\%$ and $61 \pm 11\%$ for scaffolds with ES and NTES particles, respectively, vs. $15 \pm 7\%$ for scaffolds without particles; $p < .001$ in both cases). While a trend towards decreasing cell viability over time was observed in the scaffolds with either ES or NTES particles, cell viability was lower only on days 14 and 21 in the scaffolds with NTES particles ($53 \pm 8\%$ and $61 \pm 11\%$, respectively; $p < .001$ and $p = .011$, respectively, relative to day 0). In

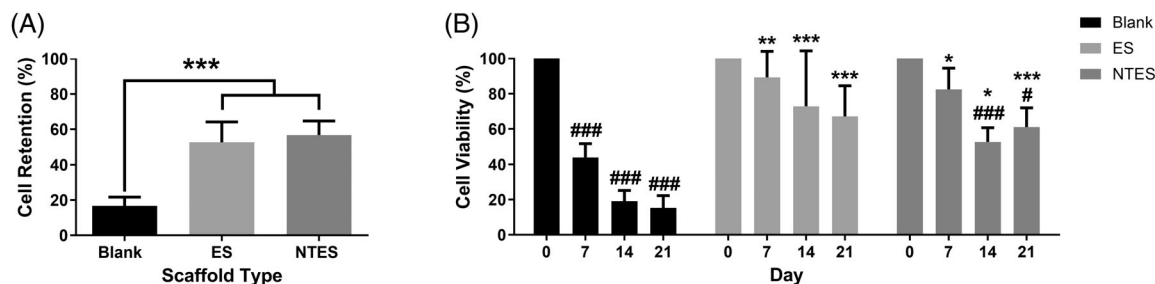


FIGURE 10 Retention and viability of mesenchymal stem cells (MSC) in scaffolds without particles (blank), or with eggshell (ES) or nanotextured eggshell (NTES) particles: (A) Cell retention after seeding on day 0; (B) Cell viability over 21 days of culture. After seeding (on day 0) and at each time point thereafter, scaffolds were incubated in medium containing alamarBlue. Fluorescence intensity was measured at excitation/emission wavelengths of 530 nm/590 nm. Cell retention (A) was calculated as a ratio between the experimentally determined number of cells in the scaffolds after seeding (on day 0) and the nominal number of cells seeded into each scaffold, and expressed as a percentage. Cell viability (B) at each time point was calculated as a percentage of the day 0 measurement. Data are presented as means \pm SEM of 4 experiments (each performed in triplicate with a different cell lot number). Statistical analysis was performed using a mixed linear model followed by the Tukey post hoc test with a single-step adjustment. An asterisk (*), a double asterisk (**), and a triple asterisk (***) indicate a significant difference with $p < .05$, $p < .01$, and $p < .001$, respectively, compared to the blank scaffolds on the same day. ALP activity did not differ significantly between the scaffolds with ES or NTES particles on the same day. A number sign (#) and a triple number sign (###) indicate a significant difference with $p < .05$ and $p < .001$, respectively, compared to the same scaffold on day 0.

contrast, cell viability in the scaffolds without particles was lower on days 7, 14, and 21 than on day 0 ($\leq 44\%$; $p < .001$ in all cases).

3.3.2 | ALP activity in the scaffolds

Levels of ALP activity in all types of scaffolds were measured over 21 days to evaluate early osteogenic differentiation (Figure 11). Results showed a time-dependent increase in ALP activity in the scaffolds with either ES or NTES particles, up to $558 \pm 164\%$ on day 21 in the scaffolds with ES particles, and up to $567 \pm 217\%$ on day 14 in the scaffolds with NTES particles ($p = .006$ and $p = .002$, respectively, relative to day 0). ALP activity in the scaffolds without particles was similar at all time points, and was lower on day 21 than in both the scaffolds with ES or NTES particles ($71 \pm 4\%$ vs. $558 \pm 164\%$ and $511 \pm 201\%$, respectively; $p = .002$ and $p = .004$, respectively).

4 | DISCUSSION

In this study, we describe the development and characterization of novel composite scaffolds, made of an alginate-chitosan hydrogel matrix containing eggshell particles, for bone tissue engineering applications. In addition, scaffolds containing either untreated ES particles or particles that had been treated with phosphoric acid to create a surface nanotexture were prepared and compared to scaffolds without particles.

4.1 | Changes in eggshell particle nanofeatures due to nanotexturing

The combination of the SEM and EDS analyses of the treated and untreated particles suggest that the granular deposits on the surface of

the NTES particles are made of calcium phosphate, a water-insoluble mineral, which can result from a chemical reaction between CaCO_3 (the main component of ES mineral, ca. 94% CaCO_3 by mass) and phosphoric acid⁴⁷ used in the nanotexturing treatment. In addition, because the granular deposits displayed a morphology similar to that of β -tricalcium phosphate (β -TCP) granules reported by Tavares et al.,⁴⁸ we hypothesize that they may be β -TCP. This interpretation is supported by the FTIR analysis of NTES particles, which revealed a singlet band around 500 cm^{-1} and a doublet band around 1000 cm^{-1} that were attributed to phosphate groups (vibrational modes ν_4 and $\nu_{1,3}$, respectively) as they were not detected when particles were treated with 0.250 M lactic acid instead of 0.250 M phosphoric acid (data not shown). Previous studies also identified such bands as phosphate signals in β -TCP granules or in hydroxyapatite that was converted from calcite.^{48,49} Overall, our SEM, EDS, and FTIR results suggest the formation of calcium phosphate deposits (possibly β -TCP) on the surface of the ES particles following phosphoric acid treatment. However, the transformation of the particles was only partial since these deposits were present only at certain locations.

Interestingly, nanotexturing with phosphoric acid appeared to have exposed occluded ES matrix proteins. Only a minimal amount of organic matter is exposed on the surface of the particles prior to nanotexturing since the proteins and organic matter of the ES matrix (about 1%–2% by mass) are occluded by the ES mineral. In addition, calcite mineral strongly absorbs incident light in FTIR spectroscopy and would prevent detection of occluded proteins, as evidenced by the absence of any protein or polysaccharide signal with the untreated particles. However, as documented by Chien et al.,¹⁸ occluded proteins that are absent from the surface of such particles can be exposed by acid etching. Therefore, during the phosphoric acid treatment, selective dissolution of calcium carbonate likely exposed proteins/organic matter, which then became detectable by FTIR spectroscopy. This would explain why the band around 1650 cm^{-1} (amide I region) and a broad band between 3500 and 2800 cm^{-1} (amide A

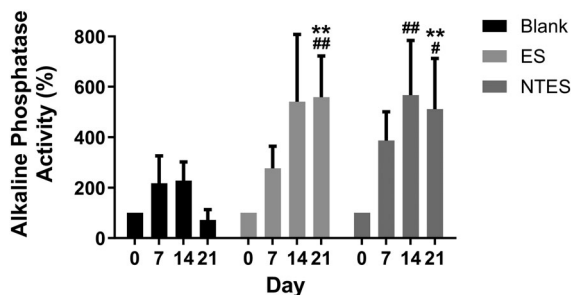


FIGURE 11 Alkaline phosphatase (ALP) activity in mesenchymal stem cells (MSC) in scaffolds without particles (blank), or with eggshell (ES) or nanotextured eggshell (NTES) particles. An aliquot of MSC lysate from each scaffold at each time point was incubated in a 96-well microplate with ALP assay buffer. Absorbance was measured at a wavelength of 405 nm and converted to ALP activity using an ALP standard curve, normalized to the number of metabolically active cells in the scaffold (determined using alamarBlue), and expressed as a percentage of the day 0 value. Data are presented as means \pm SEM of 4 experiments (each performed in triplicate with a different cell lot number). Statistical analysis was performed using a mixed linear model followed by the Tukey post hoc test with a single-step adjustment. A double asterisk (**) indicates a significant difference with $p < .01$, compared to blank scaffolds on the same day. ALP activity did not differ significantly between the scaffolds with ES and NTES particles on the same day. A number sign (#) and a double number sign (##) indicate a significant difference with $p < .05$ and $p < .01$, respectively, compared to the same scaffold on day 0.

region) were observed only after the acid treatment. Finally, in an ancillary experiment, the treatment of particles with 0.250 M lactic acid, instead of 0.250 M phosphoric acid, also led to the appearance of a band around 1650 cm^{-1} as well as a broad band between 3500 and 2800 cm^{-1} (data not shown). Since lactic acid dissolves calcium carbonate similarly to phosphoric acid, this result provides additional evidence for the exposure of amide functional groups. The emergence of these amide bands in the spectrum of NTES particles and their absence in the spectrum of ES particles suggests that the exposure of previously occluded proteins is a direct result of acid etching.

Altogether, these results point to three distinct osteogenic features of the NTES particles: 1. Nanotexture, which has been shown to facilitate MSC adherence as well as induce osteogenic differentiation via cytoskeletal disorganization^{40,50,51}; 2. Calcium phosphate mineral deposits on the particle surface, which have been shown to stimulate osteogenic differentiation^{52,53}; and 3. Proteins on the particle surface, which likely include collagen and osteopontin, both of which have been shown to induce osteogenesis in MSC.^{54–56}

4.2 | Effects of particles on scaffold microstructure, physicochemical properties, and compressive modulus

SEM analysis of the scaffolds showed that the presence of particles (either ES or NTES) led to a change in the scaffold microstructure,

and swelling tests showed an increase in porosity compared to the scaffolds without particles. These changes in microstructure and porosity are a direct result of the inclusion of either ES or NTES particles within the scaffolds and their effects on ice crystal nucleation. Indeed, the pore generation process through unidirectional freezing is significantly interrupted and hindered by the presence of the large ES or NTES particles since ice crystals cannot pass through these particles. Therefore, nucleating ice crystals move around the particles and collide with other crystals. This leads to the merging or splitting of these ice crystals, and thereby a change in microstructure and porosity.^{57,58} Interestingly, in the present study, the scaffold pore sizes were very similar in the perpendicular and parallel cross-sections, likely because of the use of a cross-linking agent (0.03% [v/v] glutaraldehyde) prior to unidirectional freezing. Indeed, a study by Nieto-Suárez et al.⁵⁹ showed very similar pore patterns between the axial and equatorial cross-sections of chitosan-gelatin scaffolds that were crosslinked with 1% [v/v] glutaraldehyde prior to unidirectional freezing.

The properties of the scaffolds with ES or NTES particles were quite similar, except for the median pore size, which was larger for the scaffolds with NTES particles. This difference was likely due to chemical interactions between the particles and the polymers when they were mixed. Indeed, an ancillary experiment showed that the addition of NTES particles (as opposed to ES particles) consistently caused the alginate solution to become more viscous (data not shown). This increase in alginate viscosity may have arisen from an increase in hydrogen bonding between exposed proteins and the polymer molecules⁵⁶ and/or an increase in calcium phosphate-induced gelation due to ionic binding between the alginate-chitosan polymer chains and the calcium phosphate on the particles.^{60–62} These interactions would lead to changes in the growth of ice crystals during freezing, and ultimately affect the distribution of pore sizes.

Finally, the CM of the scaffolds increased slightly in the presence of ES or NTES particles (possibly due to the solid particles acting as a reinforcement of the polymeric matrix⁶³), but remained much lower than that of cancellous bone. Nevertheless, the scaffold stability in solution was much improved in the presence of particles. This greater resistance to hydrolytic degradation of the scaffolds with either ES or NTES particles was likely due to particles having functional groups available for chemical bonding. Fewer or weaker chemical bonds to maintain the integrity of the scaffolds without mineral particles are expected to result in greater susceptibility to hydrolysis.⁶⁴

4.3 | Potential as a bone regeneration material

The inclusion of ES or NTES particles into the scaffolds increased MSC seeding efficiency, as demonstrated by better cell retention on day 0 and higher cell viability over 21 days of culture, compared to scaffolds without particles. Better cell retention and higher cell viability suggest improved cell adhesion inside the scaffolds containing ES or NTES particles. This may be the result of: 1. An increase in the surface roughness of pore walls due to changes in ice-crystal growth

patterns in the presence of either ES or NTES particles; and 2. A greater porosity of the scaffolds with particles. Indeed, MSC adhere better to rough surfaces,⁶⁵ and the increase in scaffold porosity in the presence of particles may have allowed greater MSC penetration during seeding as well as better diffusion of nutrients and waste during the 21 days of culture. Surprisingly, however, cell retention and viability over the 21 days of culture were not significantly higher in scaffolds with NTES particles (compared to scaffolds with ES particles). This may be due to the particle concentration inside the scaffolds being too low to allow the detection of differences in the effects of ES and NTES particles. Notwithstanding, the differences in cell retention and viability observed between the scaffolds with and without particles demonstrate that pore size and porosity remain the primary factors affecting cell viability, as previously reported.⁶⁶

The observed increases in MSC retention and viability in the scaffolds with ES or NTES particles led to the hypothesis that the scaffolds with either type of particles have greater potential as bone substitutes than the scaffolds without particles. Clearly, cell adhesion is critical since cell recruitment and retention in the scaffold are key determinants *in vivo*.⁶⁷ Additionally, adhesion is the first step in MSC differentiation into osteoblasts.⁶⁸ Therefore, ALP activity was evaluated as a marker of early osteogenic differentiation. The time-dependent increase in ALP activity observed in the scaffolds with ES or NTES particles suggests early osteogenic differentiation, which did not occur in the scaffolds without particles. While no significant differences were observed between scaffolds with the two types of particles, ALP activity appeared to increase earlier in the scaffolds with NTES particles (day 14) than in the scaffolds with ES particles (day 21). Interestingly, cell morphology, analyzed on day 21, was more cuboidal (see [Supplemental Material, Section 2](#)), also suggesting osteogenic differentiation.

Overall, the results of this study demonstrate that the scaffolds with either type of particles facilitated early osteogenic differentiation. As mentioned above, the absence of significant differences in ALP activity between the scaffolds with ES or NTES particles may be due to the low concentration of particles inside the scaffolds. This concentration was optimized to be as high as possible without compromising scaffold porosity and pore size (data not shown).

5 | CONCLUSIONS

ES and novel NTES particles were generated from chicken ES and incorporated into alginate-chitosan hydrogel scaffolds. The characterization of ES and NTES particles showed that nanotexturing treatment with phosphoric acid generated both a surface nanotexture and deposits of calcium phosphate on the particle surface. The presence of either ES or NTES particles improved the scaffold physicochemical properties, allowed better MSC retention during seeding as well as higher viability over a 21-day culture period, and facilitated early osteogenic differentiation. Therefore, alginate-chitosan hydrogel scaffolds with ES or NTES particles may represent a promising new bone substitute, especially for non-load-bearing applications.

ACKNOWLEDGMENTS

The authors thank Dr. Jianqun Wang from the Nanoimaging Facility at Carleton University (Ottawa, ON) for his assistance in the acquisition of the SEM micrographs and EDS data, as well as Ms. Kathryn Culliton from the Orthopaedic Biomechanics Laboratory at The Ottawa Hospital for her contribution to mechanical testing of the scaffolds. This work was supported by Egg Farmers of Canada (EFC) funding to Maxwell T. Hincke and Isabelle Catelas, and by a Natural Sciences and Engineering Research Council of Canada (NSERC) Discovery grant to Maxwell T. Hincke (RGPIN-2016-04410). The FTIR analysis was supported by grants from the Ministerio de Economía y Compatitividad (CGL2015-64683, Spain) and from the RNM-179 group (Junta de Andalucía, Spain) to Alejandro Rodriguez-Navarro.

DATA AVAILABILITY STATEMENT

The data that support the findings of this study are available from the corresponding authors upon reasonable request.

ORCID

Nicholas D. Calvert  <https://orcid.org/0000-0002-6637-9063>

Scott Proulx  <https://orcid.org/0009-0003-7598-5617>

Alejandro Rodriguez-Navarro  <https://orcid.org/0000-0003-2674-7383>

Tamer Ahmed  <https://orcid.org/0000-0002-6922-6193>

Eric A. Lehoux  <https://orcid.org/0000-0002-9356-7342>

Maxwell T. Hincke  <https://orcid.org/0000-0001-6134-5668>

Isabelle Catelas  <https://orcid.org/0000-0001-9784-7491>

REFERENCES

- Amini AR, Laurencin CT, Nukavarapu SP. Bone tissue engineering: recent advances and challenges. *Crit Rev Biomed Eng*. 2012;40(5):363-408. doi:10.1615/CritRevBiomedEng.v40.i5.10
- Epsicom Business Intelligence Staff. *The global orthobiologics market: players, products and technologies driving change*. Espicom Business Intelligence; 2008:2.
- Oppenheim J, Segal D, Spitzer D. Persistent iliac crest donor site pain: Independent outcome assessment. *Neurosurgery*. 2002;51(3):854-855. doi:10.1097/00006123-200209000-00060
- Hsu WK, Nickoli MS, Wang JC, et al. Improving the clinical evidence of bone graft substitute technology in lumbar spine surgery. *Global Spine J*. 2012;2(4):239-248. doi:10.1055/s-0032-1315454
- Ho-Shui-Ling A, Bolander J, Rustom LE, Johnson AW, Luyten FP, Picart C. Bone regeneration strategies: engineered scaffolds, bioactive molecules and stem cells current stage and future perspectives. *Biomaterials*. 2018;180:143-162. doi:10.1016/J.BIOMATERIALS.2018.07.017
- Buck DW, Dumanian GA. Bone biology and physiology: part I. The fundamentals. *Plast Reconstr Surg*. 2012;129(6):1314-1320. doi:10.1097/PRS.0b013e31824eca94
- Hannink G, Arts JJC. Bioresorbability, porosity and mechanical strength of bone substitutes: what is optimal for bone regeneration? *Injury*. 2011;42(Suppl. 2):S22-S25. doi:10.1016/j.injury.2011.06.008
- Tozzi G, De Mori A, Oliveira A, Roldo M. Composite hydrogels for bone regeneration. *Materials*. 2016;9(4):267. doi:10.3390/ma9040267
- Rowe DW. Osteogenesis imperfecta. *Principles of Bone Biology*. Vol 5. Elsevier; 2008:1511-1531. doi:10.1016/B978-0-12-373884-4.00008-2
- Buck DW, Dumanian GA. Bone biology and physiology. *Plast Reconstr Surg*. 2012;129(6):950e-956e. doi:10.1097/PRS.0b013e31824eca354

11. Deepthi S, Venkatesan J, Kim SK, Bumgardner JD, Jayakumar R. An overview of chitin or chitosan/nano ceramic composite scaffolds for bone tissue engineering. *Int J Biol Macromol*. 2016;93:1338-1353. doi:10.1016/j.ijbiomac.2016.03.041
12. Roy DM, Linnehan SK. Hydroxyapatite formed from coral skeletal carbonate by hydrothermal exchange. *Nature*. 1974;247:220-222. doi:10.1038/247220a0
13. Atlan G, Balmain N, Berland S, Vidal B, Lopez É. Reconstruction of human maxillary defects with nacre powder: histological evidence for bone regeneration. *Comptes Rendus de l'Académie Des Sciences - Series III - Sciences de la Vie*. 1997;320(3):253-258. doi:10.1016/S0764-4469(97)86933-8
14. Alakpa EV, Burgess KEV, Chung P, et al. Nacre topography produces higher crystallinity in bone than chemically induced osteogenesis. *ACS Nano*. 2017;11(7):6717-6727. doi:10.1021/acsnano.7b01044
15. Coringa R, de Sousa EM, Botelho JN, et al. Bone substitute made from a Brazilian oyster shell functions as a fast stimulator for bone-forming cells in an animal model. *PLoS One*. 2018;13(6):e0198697. doi:10.1371/journal.pone.0198697
16. Murakami FS, Rodrigues PO, de Campos CMT, Silva MAS. Physicochemical study of calcium carbonate₃ from egg shells. *Cienc Tecnol Aliment*. 2007;27(3):658-662. doi:10.1590/S0101-20612007000300035
17. Valletregi M, Gonzalez-Calbet JM. Calcium phosphates as substitution of bone tissues. *Prog Solid State Chem*. 2004;32(1-2):1-31. doi:10.1016/j.progsolidstchem.2004.07.001
18. Chien YC, Hincke MT, McKee MD. Avian eggshell structure and osteopontin. *Cells Tissues Organs*. 2008;189(1-4):38-43. doi:10.1159/000151374
19. Hincke MT, Chien YC, Gerstenfeld LC, McKee MD. Colloidal-gold immunocytochemical localization of osteopontin in avian eggshell gland and eggshell. *J Histochem Cytochem*. 2008;56(5):467-476. doi:10.1369/jhc.2008.950576
20. Baliga M, Davies P, Dupoirieux L. Powdered eggshell in the repair of cystic cavities of the jaw. Preliminary study. *Rev Stomatol Chir Maxillofac*. 1998;99(Suppl 1):86-88.
21. Dupoirieux L, Pourquier D, Souyris F. Powdered eggshell: a pilot study on a new bone substitute for use in maxillofacial surgery. *Journal of Cranio-Maxillofacial Surgery*. 1995;23(3):187-194. [https://doi.org/10.1016/s1010-5182\(05\)80009-5](https://doi.org/10.1016/s1010-5182(05)80009-5)
22. Gergely G, Weber F, Lukács I, et al. Preparation and characterization of hydroxyapatite from eggshell. *Ceram Int*. 2010;36(2):803-806. doi:10.1016/j.ceramint.2009.09.020
23. Kattimani V, Lingamaneni KP, Chakravarthi PS, Kumar TSS, Siddharthan A. Eggshell-derived hydroxyapatite. *J Craniofac Surg*. 2016;27(1):112-117. doi:10.1097/SCS.0000000000002288
24. Dadhich P, Das B, Pal P, et al. A simple approach for an eggshell-based 3D-printed osteoinductive multiphasic calcium phosphate scaffold. *ACS Appl Mater Interfaces*. 2016;8(19):11910-11924. doi:10.1021/acscami.5b11981
25. Jayasree R, Kumar TS, Kavya K, Nankar R, Doble M. Self setting bone cement formulations based on egg shell derived tetracalcium phosphate bioceramics. *Bioceram Dev Appl*. 2015;5(1):1-6. doi:10.4172/2090-5025.1000084
26. Uraz A, Gultekin SE, Senguven B, et al. Histologic and histomorphometric assessment of eggshell-derived bone graft substitutes on bone healing in rats. *J Clin Exp Dent*. 2013;5(1):e23-e29. doi:10.4317/jced.50968
27. Sun J, Tan H. Alginate-based biomaterials for regenerative medicine applications. *Materials*. 2013;6(4):1285-1309. doi:10.3390/ma6041285
28. Upadhyaya L, Singh J, Agarwal V, Tewari RP. Biomedical applications of carboxymethyl chitosans. *Carbohydr Polym*. 2013;91(1):452-466. doi:10.1016/j.carbpol.2012.07.076
29. Saravanan S, Leena RS, Selvamurugan N. Chitosan based biocomposite scaffolds for bone tissue engineering. *Int J Biol Macromol*. 2016; 93:1354-1365. doi:10.1016/j.ijbiomac.2016.01.112
30. Yue S, He H, Li B, Hou T. Hydrogel as a biomaterial for bone tissue engineering: a review. *Nanomaterials*. 2020;10(8):1511. doi:10.3390/nano10081511
31. Gyles DA, Castro LD, Silva JOC, Ribeiro-Costa RM. A review of the designs and prominent biomedical advances of natural and synthetic hydrogel formulations. *Eur Polym J*. 2017;88(1):373-392. doi:10.1016/j.eurpolymj.2017.01.027
32. Drury JL, Mooney DJ. Hydrogels for tissue engineering: scaffold design variables and applications. *Biomaterials*. 2003;24(24):4337-4351. doi:10.1016/S0142-9612(03)00340-5
33. Lan Levengood S, Zhang M. Chitosan-based scaffolds for bone tissue engineering sheeny. *J Mater Chem B Mater Biol Med*. 2015;2(21): 3161-3184. doi:10.1039/C4TB00027G.Chitosan-based
34. Shi C, Hou X, Zhao D, Wang H, Guo R, Zhou Y. Preparation of the bio-glass/chitosan-alginate composite scaffolds with high bioactivity and mechanical properties as bone graft materials. *J Mech Behav Biomed Mater*. 2022;126:105062. doi:10.1016/J.JMBBM.2021.105062
35. Wu X, Gauntlett O, Zhang T, et al. Eggshell microparticle reinforced scaffolds for regeneration of critical sized cranial defects. *ACS Appl Mater Interfaces*. 2021;13(51):60921-60932. doi:10.1021/ACSAMI.1C19884/ASSET/IMAGES/MEDIUM/AM1C19884_0006.GIF
36. Wu X, Stroll SI, Lantigua D, Suvarnapathaki S, Camci-Unal G. Eggshell particle-reinforced hydrogels for bone tissue engineering: an orthogonal approach. *Biomater Sci*. 2019;7(7):2675-2685. doi:10.1039/C9BM00230H
37. Asghar W, Kim YT, Ilyas A, Sankaran J, Wan Y, Iqbal SM. Synthesis of nano-textured biocompatible scaffolds from chicken eggshells. *Nanotechnology*. 2012;23(47):475601. doi:10.1088/0957-4484/23/47/475601 and references therein.
38. Islam M, Sajid A, Mahmood MAI, et al. Nanotextured polymer substrates show enhanced cancer cell isolation and cell culture. *Nanotechnology*. 2015;26(22):225101. doi:10.1088/0957-4484/26/22/225101
39. Klos A, Sedao X, Itina TE, et al. Ultrafast laser processing of nano-structured patterns for the control of cell adhesion and migration on titanium alloy. *Nanomaterials*. 2020;10(5):864. doi:10.3390/nano10050864
40. Müller P, Bulnheim U, Diener A, et al. Calcium phosphate surfaces promote osteogenic differentiation of mesenchymal stem cells. *J Cell Mol Med*. 2008;12(1):281-291. doi:10.1111/j.1582-4934.2007.00103.x
41. Song X, Zhu C, Fan D, et al. A novel human-like collagen hydrogel scaffold with porous structure and sponge-like properties. *Polymers (Basel)*. 2017;9(12):638. doi:10.3390/polym9120638
42. Grabska-Zielińska S, Sionkowska A, Reczyńska K, Pamuła E. Physicochemical characterization and biological tests of collagen/silk fibroin/chitosan scaffolds cross-linked by dialdehyde starch. *Polymers (Basel)*. 2020;12(2):372. doi:10.3390/polym12020372
43. Bas O, De-Juan-Pardo EM, Meinert C, et al. Biofabricated soft network composites for cartilage tissue engineering. *Biofabrication*. 2017;9(2):1-11. doi:10.1088/1758-5090/aa6b15
44. Sekine W, Haraguchi Y. Thickness limitation and cell viability of multi-layered cell sheets and overcoming the diffusion limit by a porous-membrane culture insert. *J Biochips Tissue Chips*. 2011;1(1):1-9. doi:10.4172/2153-0777.S1-007
45. Shum LC, White NS, Mills BN, de Mesy Bentley KL, Eliseev RA. Energy metabolism in mesenchymal stem cells during osteogenic differentiation. *Stem Cells Dev*. 2016;25(2):114-122. doi:10.1089/scd.2015.0193
46. R Core Team (2021). R: A language and environment for statistical computing. R Foundation for Statistical Computing, Vienna, Austria. URL <https://www.R-project.org/>.
47. Nancollas GH, Sawada K, Schuttringer E. Mineralization reactions involving calcium carbonates and phosphates. *Biomineralization and Biological Metal Accumulation*. Springer; 1983:155-169. doi:10.1007/978-94-009-7944-4_14

48. Tavares Ddos S, Castro Lde O, Soares GD, Alves GG, Granjeiro JM. Synthesis and cytotoxicity evaluation of granular magnesium substituted β -tricalcium phosphate. *J Appl Oral Sci.* 2013;21(1):37-42. doi:[10.1590/1678-7757201302138](https://doi.org/10.1590/1678-7757201302138)
49. Boyan BD, Cheng A, Olivares-Navarrete R, Schwartz Z. Implant surface design regulates mesenchymal stem cell differentiation and maturation. *Adv Dent Res.* 2016;28(1):10-17. doi:[10.1177/0022034515624444](https://doi.org/10.1177/0022034515624444)
50. Roberts JN, Sahoo JK, McNamara LE, et al. Dynamic surfaces for the study of mesenchymal stem cell growth through adhesion regulation. *ACS Nano.* 2016;10(7):6667-6679. doi:[10.1021/acs.nano.6b01765](https://doi.org/10.1021/acs.nano.6b01765)
51. Dalby MJ, Gadegaard N, Tare R, et al. The control of human mesenchymal cell differentiation using nanoscale symmetry and disorder. *Nat Mater.* 2007;6(12):997-1003. doi:[10.1038/nmat2013](https://doi.org/10.1038/nmat2013)
52. Li Y, Jiang T, Zheng L, Zhao J. Osteogenic differentiation of mesenchymal stem cells (MSCs) induced by three calcium phosphate ceramic (CaP) powders: a comparative study. *Mater Sci Eng C.* 2017;80:296-300. doi:[10.1016/j.msec.2017.05.145](https://doi.org/10.1016/j.msec.2017.05.145)
53. Singh A, Gill G, Kaur H, Amhmed M, Jakhu H. Role of osteopontin in bone remodeling and orthodontic tooth movement: a review. *Prog Orthod.* 2018;19(1):18. doi:[10.1186/s40510-018-0216-2](https://doi.org/10.1186/s40510-018-0216-2)
54. Chen Q, Shou P, Zhang L, et al. An Osteopontin-integrin interaction plays a critical role in directing adipogenesis and osteogenesis by mesenchymal stem cells. *Stem Cells.* 2014;32(2):327-337. doi:[10.1002/stem.1567](https://doi.org/10.1002/stem.1567)
55. Lukasova V, Buzgo M, Sovkova V, Dankova J, Rampichova M, Amler E. Osteogenic differentiation of 3D cultured mesenchymal stem cells induced by bioactive peptides. *Cell Prolif.* 2017;50(4):1-12. doi:[10.1111/cpr.12357](https://doi.org/10.1111/cpr.12357)
56. O'Brien FJ, Harley BA, Yannas IV, Gibson L. Influence of freezing rate on pore structure in freeze-dried collagen-GAG scaffolds. *Biomaterials.* 2004;25(6):1077-1086. doi:[10.1016/S0142-9612\(03\)00630-6](https://doi.org/10.1016/S0142-9612(03)00630-6)
57. Deville S. Freezing as a path to build complex composites. *Science.* 2006;311(5760):515-518. doi:[10.1126/science.1120937](https://doi.org/10.1126/science.1120937)
58. Nieto-Suárez M, López-Quintela MA, Lazzari M. Preparation and characterization of crosslinked chitosan/gelatin scaffolds by ice segregation induced self-assembly. *Carbohydr Polym.* 2016;141:175-183. doi:[10.1016/j.carbpol.2015.12.064](https://doi.org/10.1016/j.carbpol.2015.12.064)
59. Lin YH, Liang HF, Chung CK, Chen MC, Sung HW. Physically cross-linked alginate/N,O-carboxymethyl chitosan hydrogels with calcium for oral delivery of protein drugs. *Biomaterials.* 2005;26(14):2105-2113. doi:[10.1016/j.biomaterials.2004.06.011](https://doi.org/10.1016/j.biomaterials.2004.06.011)
60. Nokhodchi A, Tailor A. In situ cross-linking of sodium alginate with calcium and aluminum ions to sustain the release of theophylline from polymeric matrices. *Il Farmaco.* 2004;59(12):999-1004. doi:[10.1016/j.farmac.2004.08.006](https://doi.org/10.1016/j.farmac.2004.08.006)
61. Alves Cardoso D, Van Den Beucken JJJ, Both LLH, Bender J, Jansen JA, Leeuwenburgh SCG. Gelation and biocompatibility of injectable alginate-calcium phosphate gels for bone regeneration. *J Biomed Mater Res A.* 2014;102(3):808-817. doi:[10.1002/jbm.a.34754](https://doi.org/10.1002/jbm.a.34754)
62. Torres-Sanchez C, Al Mushref FRA, Norrito M, Yendall K, Liu Y, Conway PP. The effect of pore size and porosity on mechanical properties and biological response of porous titanium scaffolds. *Mater Sci Eng C.* 2017;77:219-228. doi:[10.1016/j.msec.2017.03.249](https://doi.org/10.1016/j.msec.2017.03.249)
63. Ren D, Yi H, Wang W, Ma X. The enzymatic degradation and swelling properties of chitosan matrices with different degrees of N-acetylation. *Carbohydr Res.* 2005;340(15):2403-2410. doi:[10.1016/j.carres.2005.07.022](https://doi.org/10.1016/j.carres.2005.07.022)
64. Tillotson M, Logan N, Brett P. Osteogenic stem cell selection for repair and regeneration. *Bone Rep.* 2016;5:22-32. doi:[10.1016/j.bonr.2016.01.003](https://doi.org/10.1016/j.bonr.2016.01.003)
65. Murphy CM, O'Brien FJ. Understanding the effect of mean pore size on cell activity in collagen-glycosaminoglycan scaffolds. *Cell Adhes Migr.* 2010;4(3):377-381. doi:[10.4161/cam.4.3.11747](https://doi.org/10.4161/cam.4.3.11747)
66. Khalili A, Ahmad M. A review of cell adhesion studies for biomedical and biological applications. *Int J Mol Sci.* 2015;16(8):18149-18184. doi:[10.3390/ijms160818149](https://doi.org/10.3390/ijms160818149)
67. Wang YK, Chen CS. Cell adhesion and mechanical stimulation in the regulation of mesenchymal stem cell differentiation. *J Cell Mol Med.* 2013;17(7):823-832. doi:[10.1111/jcmm.12061](https://doi.org/10.1111/jcmm.12061)
68. Nassif N, Martineau F, Syzgantseva O, et al. In vivo inspired conditions to synthesize biomimetic hydroxyapatite. *Chem Mater.* 2010;22(12):3653-3663. doi:[10.1021/cm903596q](https://doi.org/10.1021/cm903596q)

SUPPORTING INFORMATION

Additional supporting information can be found online in the Supporting Information section at the end of this article.

How to cite this article: Calvert ND, Proulx S, Rodriguez-Navarro A, et al. Development of hydrogel-based composite scaffolds containing eggshell particles for bone regeneration applications. *J Biomed Mater Res.* 2024;112(1):e35296. doi:[10.1002/jbm.b.35296](https://doi.org/10.1002/jbm.b.35296)